



Artificial intelligence-assisted projection-resolved optical coherence tomographic angiography (aiPR-OCTA)

JIE WANG,¹ TRISTAN T. HORMEL,¹ STEVEN T. BAILEY,¹ THOMAS S. HWANG,¹ AND YALI JIA^{1,2,*}

¹Casey Eye Institute, Oregon Health & Science University, Portland, Oregon, USA

²Department of Biomedical Engineering, Oregon Health & Science University, Portland, Oregon, USA

*jiaya@ohsu.edu

Abstract: We improved voxel-wise projection-resolved optical coherence tomographic angiography (PR-OCTA) using artificial intelligence. For generating a high-quality ground truth, our approach involved graders editing the flow signal to achieve an optimal appearance in the inner/outer retina and choroid through a rule-based PR-OCTA algorithm, ensuring the preservation of *in situ* flow signals (ground truth) while removing residual artifacts. The developed model employs a convolutional neural network to generate projection-resolved OCTA volumes from structural OCT and OCTA inputs. We evaluated the artificial intelligence PR-OCTA (aiPR-OCTA) algorithm on 126 normal eyes by assessing structural similarity (SSIM), flow signal-to-noise ratio (fSNR), and residual artifact strength. Compared to the existing state-of-the-art rule-based PR-OCTA algorithm, aiPR-OCTA demonstrated superior artifact removal, better preservation of flow signals, and accurate maintenance of anatomical details at the capillary scale. Additionally, it achieved a higher fSNR and reduced background artifacts.

© 2025 Optica Publishing Group under the terms of the [Optica Open Access Publishing Agreement](#)

1. Introduction

Optical Coherence Tomographic Angiography (OCTA) represents a significant advancement stemming from the OCT technique [1,2]. By capturing continuous B-scans at identical locations, OCTA detects variations in the OCT signal induced by moving blood cells, thereby enabling imaging of vessels. This technique exploits the signal changes caused by moving blood cells in contrast to the relatively stable signals from static retinal tissue. In ophthalmology, OCTA has emerged as a valuable tool, offering non-invasive, dye-free, rapid, and depth-resolved imaging of retinal and choroidal circulatory networks down to capillary-level resolution. This capability holds promise for identifying early biomarkers and accurately assessing retinal vascular diseases. Leveraging OCTA's depth-resolved imaging, segmentation of anatomic layers within OCTA volumes facilitates *en face* visualization of retinal vasculature and vascular pathologies within specific anatomic regions. For example, non-perfusion area (NPA) within the superficial vascular complex (SVC), intermediate capillary plexus (ICP), deep capillary plexus (DCP) in the inner retina [3], and macular neovascularization (MNV) in the outer retina can be visualized [4–7]. Clinical studies have demonstrated the significant potential of OCTA for replacing invasive imaging modalities like fluorescein angiography and indocyanine green angiography [5].

However, the originally proposed OCTA faces a significant limitation in projection artifacts [8], which pose a particular challenge as they generate false flow signals, mimicking the morphology of superficial vasculature in deeper anatomical layers. These artifacts can potentially lead to the misinterpretation of vascular pathologies in the deep vascular plexus and MNV in the outer retina. The initial efforts aimed at mitigating projection artifacts were slab-subtraction methods involving the subtraction of deeper *en face* angiograms from anterior angiograms [4,9]. However, these methods introduced drawbacks such as generating negative shadows in posterior slabs

and disrupting vessel continuity, negatively impacting the accurate quantification of vascular changes. The slab subtraction-based method also only removes projection artifacts in *en face* images, rather than voxel-by-voxel, which means that it does not apply to cross-sectional images. The lack of this capability has major disadvantages, such as preventing the determination of MNV type. To avoid these issues we previously developed a voxel-by-voxel approach by (1) analyzing the normalized flow signal, whereby projection artifact signals are lower than the anatomic flow signal [10]; (2) suppressing projection artifacts by enhancing the vascular signal in OCT and then multiplying it with the uncorrected flow signal, based on the fact that blood cell reflectance is higher than that of surrounding tissue [11]; and (3) applying a signal attenuation model (called signal attenuation-compensated PR-OCTA, sacPR-OCTA) that considers both the natural reflectivity of tissue and the attenuation of the reflectance signal due to light scattering and absorptions [12]. Compared to earlier methods, the latest sacPR-OCTA boosts the *in situ* flow signal under large vessels instead of excessively processing or removing it. Both the slab subtraction-based and volumetric methods use linear models, although this simplification is unlikely to realistically capture projection artifact dynamics. Instead, a complex, non-linear model is more likely to reasonably represent the intricate relationship between *in-situ* flow, reflectance, and uncorrected flow signals.

Here, our group pioneers an artificial intelligence-assisted approach that utilizes a deep learning model to replicate possible non-linear components of the relationship between OCT and OCTA signals, aiming to restore the *in-situ* flow signal from the uncorrected OCTA data. Exploring a precise equation for the non-linear mathematical modeling of PR-OCTA is a difficult task due to the interplay between both the structural and flow signals. These factors may involve thresholding settings for structural OCT or OCTA generation, data normalization, various pathologies, noise, and more, with each factor contributing differently to each scan. To account for these details, we graded a large and complex dataset to train the designed CNN model, enabling it to learn the general principles for restoring the *in-situ* flow signal by leveraging the non-linear modeling capabilities inherent in deep learning networks.

2. Methods

2.1. Retinal layer segmentation and preprocessing

Retinal layer segmentation is an essential pre-processing step for generating the ground truth and evaluating performance as well as generating the *en face* angiograms that are normally analyzed in OCTA. A graph search-based algorithm, utilizing the image gradients as the path weights to search the shortest path from one side to the other, segmented the boundaries between the vitreous and the inner limiting membrane (ILM); the ganglion cell layer (GCL) and the inner plexiform layer (IPL); IPL and the outer plexiform layer (OPL); OPL and the outer nuclear layer (ONL); and Bruch's membrane (BM) from structural OCT volumes [13]. Segmentation errors were manually corrected using our custom Center for Ophthalmic Optics & Lasers Lab OCTA reading toolkit (COOL-ART) software with intelligent manual correction. We generated maximum projection *en face* OCT angiograms of the superficial vascular complex (SVC), comprising the inner 80% of the ganglion cell complex (GCC); the intermediate capillary plexus (ICP), comprising the outer 20% of the GCC and inner 50% of the INL; the deep capillary plexus (DCP), comprising the outer 50% of the INL through the OPL; the outer retina comprising the slab between the outer boundary of OPL and BM; and the choriocapillaris (CC), comprising the slab from BM to 10 μm posterior to BM [3].

2.2. Projection artifacts in original OCTA

Projection artifacts manifest as tails in the cross-sections and mirror vascular patterns from the superficial layers and extending into the deep anatomical slabs in *en face* images (Fig. 1). The

detected OCTA value $S(z)$ of the voxel at the position z comprises the components of the in situ flow signal $S_t(z)$, projection artifacts $S_a(z)$, and noise $n(z)$:

$$S(z) = f [S_t(z), S_a(z), n(z)]. \quad (1)$$

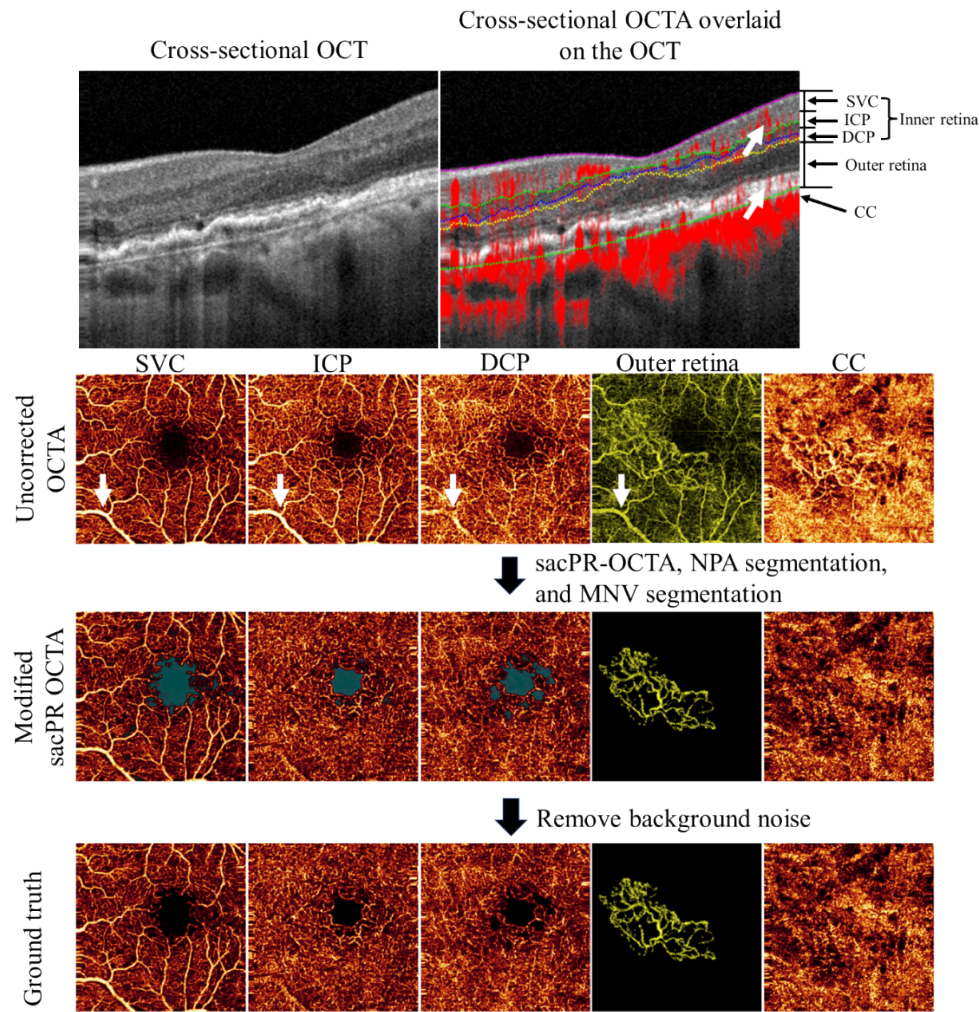


Fig. 1. Illustration of PR-OCTA ground truth generation using the optical coherence tomographic angiography (OCTA) data from an eye diagnosed with age-related macular degeneration. Row 1: The cross-sectional OCT and uncorrected OCTA (red); Row 2: The slab-specific *en face* angiograms of the superficial vascular complex (SVC), intermediate capillary plexus (ICP), deep capillary plexus (DCP) in the inner retina exhibit ischemia, macular neovascularization (MNV) in the outer retina, and choriocapillaris (CC). The projection artifacts (highlighted by the white arrow in Row 1) duplicate the vascular patterns from the superficial slab. The non-perfusion area (NPA, indicated by transparent light blue regions) in SVC, ICP, and DCP, as well as MNV in the outer retina, was segmented to eliminate the background noise. The white arrows highlighted the projection artifacts in cross-sectional OCTA (Row 1) and the *en face* images (Row 2). The dynamic display range, defined as [2.5th percentile, 97.5th percentile], was applied to generate uniformly displayed images, mitigating the brightness variation caused by differences in signal strength variation.

Establishing a precise model f for real flow signal restoration is impractical due to its complexity and variability across different voxels. To simplify the model, the in situ flow signal $S_t(z)$ can be restored from the detected OCTA value by calculating the proportions using

$$S_t(z) = p(z)S(z) \quad (2)$$

Based on our previous research [12], we understand that the in situ flow signal and projection artifact correlate with the structural OCT $R(z)$ and detected flow signal $S(z)$. Therefore, we can deduce that the proportions can be estimated by:

$$p(z) = g[R(z), S(z)] \quad (3)$$

Establishing a precise model g is impractical, therefore, we used the AI model to simulate the restoration of the in situ flow signal. This allows for complex non-linear relationships to be learned by deep learning model, which can approximate g by relying on a large number of hidden variables. Our model was trained to estimate $p(z)$ from input structural OCT and OCTA volumes.

2.3. Ground truth generation

The PR-OCTA ground truth was generated by allowing graders to adjust parameters within the sacPR-OCTA algorithm to independently optimize the appearance of flow signal in the anatomic vascular slabs of SVC, ICP, DCP outer retina, CC, and the area below the large vessels. In this way, (1) residual artifacts were removed while (2) real flow signals from posterior vessels were retained (Fig. 1(Row 3)), (3) pathological macular neovascularization (MNV) detected by an automated deep learning model was preserved [6,14], and (4) background noise in the detected nonperfusion area was cleaned up (Fig. 1(Row 4)) [15].

2.4. Network architecture

The aiPR-OCTA convolutional neural network (CNN) model (Fig. 2), as proposed, receives OCT and OCTA volumes as input. These volumes are partitioned into cross-sections and passed through the initial convolutional layers for feature extraction. OCT and OCTA features are merged through element-wise multiplication. Each convolution block includes a convolution layer, batch normalization layers, and a ReLU activation layer. As the model progresses deeper, features are down-sampled along A-lines to enhance feature extraction, considering information from both the anterior and inferior aspects. The image size remains consistent in the fast direction throughout the feature extraction process to maintain vasculature resolution. The 2D weight maps at all feature extraction levels are generated from the most significant (maximum projection) and populous (mean projection) elements, which are then concatenated to form the proportion map described in Eq. (3). The final weight map is multiplied with the merged features to generate the final output of the PR-OCTA. The inputs of the designed model are uncorrected OCT and OCTA volumes that are normalized to 0 to 1 based on their minimum and maximum, and the output PR-OCTA volume with values varying between 0 and 1.

2.5. Training and implementation

The loss function is the key to guiding the model's convergence during the training progress. Several losses, including (1) mean square error (MSE) between the output and ground truth, (2) structural similarity (SSIM) of the ICP and DCP to their anterior slabs, according to

$$\begin{cases} MSE(y_1, y_2) = \frac{1}{N} \sum_{i=1}^N [y_1(i) - y_2(i)]^2 \\ SSIM(y_1, y_2) = \frac{(2\mu_1\mu_2+c_1)(2\sigma_{12}+c_2)}{(\mu_1^2+\mu_2^2+c_1)(\sigma_1^2+\sigma_2^2+c_2)} \end{cases} \quad (4)$$

y_1 and y_2 are two images 1 and 2, respectively; The intensity at the pixel i in images 1 and 2 is written as $y_1(i)$ and $y_2(i)$, respectively; μ_1 and μ_2 represent the mean intensity of images 1 and

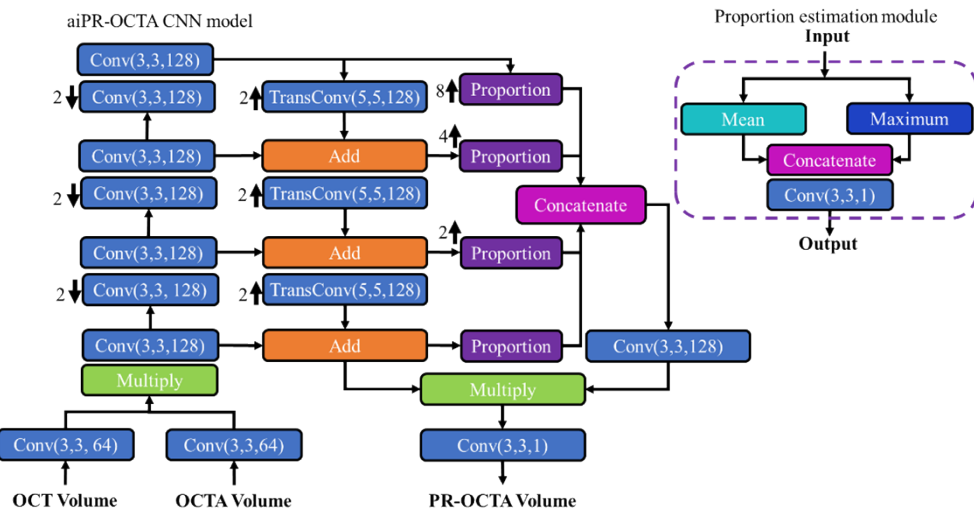


Fig. 2. The proposed aiPR-OCTA CNN model. The inputs are the original detected OCT and uncorrected OCTA signal. These inputs are multiplied and then encoded using several layers of convolutions. Outputs from convolutions are added and proportions, which correspond to $p(z)$ in Eq. (3), are then concatenated and multiplied to produce the final projection resolved (PR-OCTA) output. The numbers within the convolution block represent the kernel size in terms of width, height, and the number of kernels. The down and up arrows indicate downsampling and upsampling along the A-line, respectively, with the values 2, 4, and 8 representing the corresponding sampling rates.

2, respectively; σ_1^2 and σ_2^2 represent the variance of images 1 and 2, respectively; $c_1 = 0.0001$; and $c_2 = 0.0009$. A SSIM coefficient is bounded between 0 and 1, with an SSIM value of 0 indicating no correlation, and a SSIM value of 1 indicating perfect correlation. The average of MSE and SSIM was employed as the total loss to control the training process.

The proposed aiPR-OCTA CNN model was implemented using Tensorflow on the device with an intel i9-10980XE@3.0 GHz, DDR4 256GB, and Nvidia Quadro RTX 8000 graphics card (4608 CUDA cores, 48 GB GDDR6 memory). The training batch size is 13, and the number of epochs is 21.

3. Results

In this study, a total of 4600 OCTA scans from 708 eyes were collected for training, including 3224 AMD scans and 1376 DR scans. Additionally, 126 OCTA scans from 126 healthy eyes were collected to evaluate the performance using sacPR-OCTA and aiPR-OCTA. All OCTA scans were acquired in the 3 × 3-mm central macular area.

3.1. Evaluation on healthy eyes

3.1.1. Visual examination

Visual examination reveals that in contrast to the uncorrected OCTA (Fig. 3(A1-F1)), aiPR-OCTA effectively eliminated projection artifacts volumetrically (Fig. 3(A4-F4)).

In the uncorrected OCTA, projection artifacts manifest as “tails” extending downward from vessels in cross-section (Fig. 3(F1)), projecting vascular patterns from the superficial vascular complex (SVC) (Fig. 3(A1)) to the intermediate capillary plexus (ICP) (Fig. 3(B1)), the deep capillary plexus (DCP) (Fig. 3(C1)), the outer retina (which is typically avascular; Fig. 3(D1)), and the choriocapillaris (Fig. 3(E1)) in *en face* angiograms. In contrast to the rule-based sacPR-OCTA

algorithm (Fig. 3(A2-F2)), the aiPR-OCTA algorithm (Fig. 3(A4-F4)) retained more flow signal and exhibited more complete microvascular patterns in all deeper vascular plexuses, including the ICP (Fig. 3(B4)), DCP (Fig. 3(C4)), and CC (Fig. 3(E4)), particularly in areas posterior to large vessels. It also more effectively suppressed projection artifacts, resulting in a markedly cleaner outer retinal slab. Furthermore, the uniformity of the CC vasculature (Fig. 3(E4)) was enhanced with aiPR-OCTA compared to uncorrected OCTA (Fig. 3(E1)) and sacPR-OCTA (Fig. 3(E2)), bringing it closer to the histological description of the CC. This improvement increases the likelihood that biomarkers based on the CC accurately reflect changes in this layer. Notably, the negative large vessel shadows observed in the rule-based method (Fig. 3(E2)) were largely ameliorated with aiPR-OCTA (Fig. 3(E4)).

3.1.2. Quantitative evaluation – vascular similarity to superficial plexuses

We measured the vascular similarity using the structural similarity (SSIM) [16] according to the Eq. (4).

SSIM measures the removal of duplicated vascular patterns in the deeper slabs. An SSIM value close to 0 demonstrates better performance for removing the projection artifacts. An SSIM value close to unity demonstrates worse performance for removing the projection artifacts. The circular area with 1-mm diameter centered on the FAZ was excluded from evaluations. Projection artifacts in the uncorrected OCTA produce a high SSIM in the ICP and DCP (Table 1). Compared to the uncorrected OCTA, the vascular similarity was significantly reduced ($p < 0.01$, one sided t-test) with rule-based sacPR-OCTA and aiPR-OCTA (Table 1). Compared to sacPR-OCTA, the aiPR-OCTA showed a significant reduction of vascular similarity in the ICP ($p < 0.01$, t-test). The SSIM of aiPR-OCTA was further significantly improved compared to the sacPR-OCTA in the bothe ICP and DCP ($p < 0.01$, t-test), showing in the enface images that the duplicated vascular patterns were removed. The lower similarity in the DCP achieved by aiPR-OCTA indicates better performance in removing projection artifacts and reserving *in situ* flow signals. Visual inspection indicates the capillary networks match the evaluated values (Fig. 3).

Table 1. Comparison of structural similarity (SSIM) between the SVC and the deeper vascular plexuses using uncorrected OCTA, rule-based signal attenuation-compensated projection-resolved OCTA (sacPR-OCTA), and artificial intelligence-assisted PR-OCTA (aiPR-OCTA).^a

	Uncorrected OCTA	sacPR-OCTA	aiPR-OCTA
ICP	0.70 ± 0.03	0.37 ± 0.08	0.25 ± 0.05
DCP	0.61 ± 0.05	0.32 ± 0.08	0.19 ± 0.05

^aICP: Intermediate capillary plexus; DCP: Deep capillary plexus

3.1.3. Quantitative evaluation – flow signal-to-noise ratio

Flow signal-to-noise ratio (fSNR) was calculated from the angiograms [1,12] as

$$fSNR = \frac{M_{Vessel} - M_{FAZ}}{\sigma_{FAZ}} \quad (5)$$

where, M_{Vessel} and M_{FAZ} are the mean values of the vessel area excluding the FAZ area with 1 mm diameter and FAZ within the 1 mm diameter area.

A higher fSNR value indicates better image quality. Compared to the rule-based sacPR-OCTA, aiPR-OCTA significantly improved image quality in the deeper slabs ($p < 0.01$), because the AI model also removed the background noise during the projection artifacts removal. For example, the FAZ also is cleaned with the AI approach (Fig. 3(A4-C4)). Table 2 shows that the fSNR in sacPR-OCTA is lower than that in uncorrected OCTA. This can be explained by the fact that the

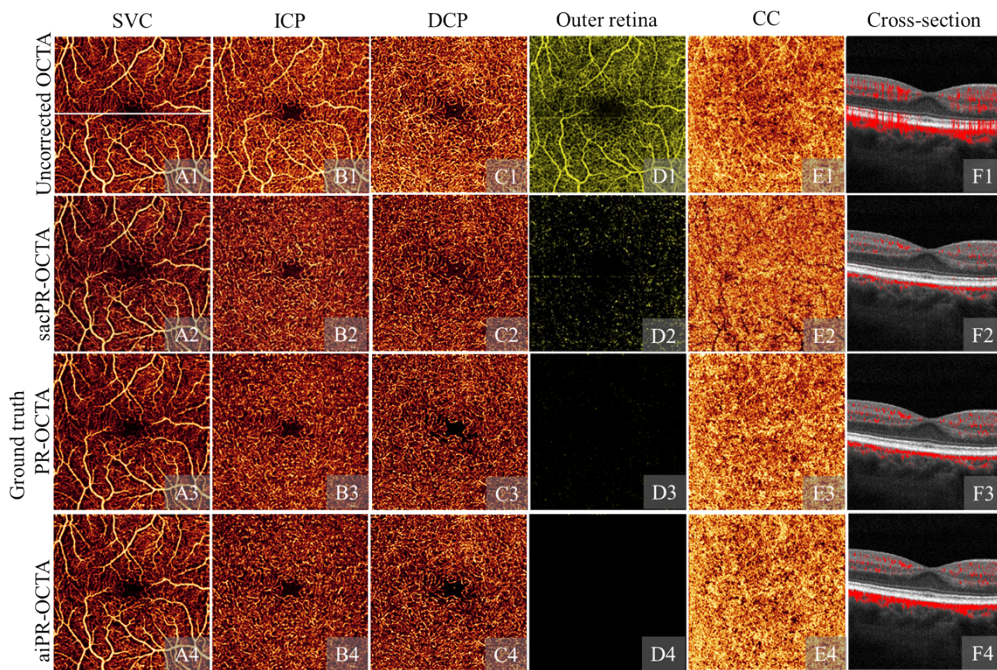


Fig. 3. Macular capillaries from a healthy eye demonstrated by the original or uncorrected OCTA (row 1), rule-based signal attenuation-compensated projection-resolved OCTA (sacPR-OCTA; row 2), ground truth projection-resolved OCTA (PR-OCTA, row 3), and the artificial intelligence-assisted projection-resolved OCTA (aiPR-OCTA, row 4) showing *en face* OCT angiogram of the superficial vascular plexus (SVC, column A), the intermediate capillary plexus (ICP, column B), the deep capillary plexus (DCP, column C), the outer retina (column D) and the choriocapillaris (CC, column E), and the cross-sectional structural OCT overlaid with color-coded flow signal (column F, red) at the position indicated by the white line in A1. The aiPR-OCTA removed projection artifacts in deeper slabs showing integrity capillary networks in the ICP and DCP, artifacts-free outer retina, and uniform CC. With rule-based sacPR-OCTA the flow signal is reduced under the larger vessels in the CC (E2, E4). These overprocessing artifacts are absent in the proposed aiPR-OCTA (E4), which shows uniform vascular patterns in the CC and clean outer retina. The SSIM values between the ICP and SVC are 0.57, 0.11, 0.10, and 0.11 for the original OCTA, sacPR-OCTA, ground truth, and aiPR-OCTA, respectively. The SSIM values between DCP and SVC + ICP are 0.35, 0.11, 0.09, and 0.11 for original OCTA, sacPR-OCTA, ground truth, and aiPR-OCTA, respectively. Compared to the sacPR, aiPR-OCTA demonstrates a clean outer retina and even CC without overprocessing under large vessels. The dynamic display range, defined as [2.5th percentile, 97.5th percentile], was applied to generate uniformly displayed images, mitigating the brightness variation caused by differences in signal strength variation.

flow signal in uncorrected OCTA appears stronger due to the inclusion of projection artifacts. In sacPR-OCTA, the *in situ* flow signal is restored by multiplying the uncorrected flow signal with the estimated *in situ* flow signal proportion, which varies from 0 to 1. However, sacPR-OCTA is not able to completely remove background noise. Consequently, the ratio of preserved flow signal to background noise is lower in sacPR-OCTA compared to the uncorrected OCTA signal.

Table 2. Comparison of flow signal-to-noise (fSNR) in the deeper vascular plexuses using uncorrected OCTA, rule-based signal attenuation-compensated projection-resolved OCTA (sacPR-OCTA), and artificial intelligence-assisted PR-OCTA (aiPR-OCTA).^a

	Uncorrected OCTA	sacPR-OCTA	aiPR-OCTA
ICP	7.40 ± 3.51	5.51 ± 2.95	21.51 ± 24.83
DCP	4.52 ± 1.38	2.89 ± 1.42	11.11 ± 12.94

^aICP: Intermediate capillary plexus; DCP: Deep capillary plexus

3.1.4. Quantitative evaluation – residual projection artifact signal strength in the outer retina

Residual projection artifact signal strength (S_{RA}) in the outer retina [11], which is important for the accurate detection and quantification of macular neovascularization (MNV) in the normally avascular outer retina, was evaluated by

$$S_{RA} = \frac{M_{outer} + 3 \times \sigma_{outer}}{M_{inner} + 3 \times \sigma_{inner}} \quad (6)$$

where, M_{outer} and M_{inner} are mean and σ_{outer} and σ_{inner} are standard deviation in the outer and inner retina, respectively.

The lower S_{RA} demonstrates that both the rule-based sacPR-OCTA and aiPR-OCTA effectively eliminated the projection artifacts in the outer retina of healthy eyes (Table 3), which aligns with the visual inspection of the *en face* images, where sacPR-OCTA exhibited weak random background noise and aiPR-OCTA presented a clean background.

Table 3. Comparison of residual projection artifact strength (S_{RA}) in the deeper vascular plexuses using uncorrected OCTA, rule-based signal attenuation-compensated projection-resolved OCTA (sacPR-OCTA), and artificial intelligence-assisted PR-OCTA (aiPR-OCTA).

Uncorrected OCTA	sacPR-OCTA	aiPR-OCTA
0.91 ± 0.10	0.32 ± 0.08	0.11 ± 0.05

3.2. Evaluation on pathological eyes

3.2.1. Preservation of macular neovascularization

Macular neovascularization (MNV) involves the development of abnormal vessels in the outer retina, leading to vision impairment through exudation, hemorrhage, fibrosis, and tissue damage [17–21]. While OCTA was initially proposed for MNV detection, its efficacy was hindered by the nearby highly reflective retinal pigment epithelium, resulting in prominent projection artifacts (Fig. 4(D1)). These artifacts pose a challenge as they can obscure genuine MNV or be mistakenly interpreted as MNV by clinicians. Given the clinical importance of quantifying MNV progression, the presence of artifacts severely impedes accurate quantification. Although the rule-based sacPR-OCTA algorithms (Fig. 4(D2)) could mitigate these artifacts to some extent, the *in situ* MNV flow signal remains relatively weak, potentially complicating MNV quantification. Furthermore, MNV-related projection artifacts in the choriocapillaris (CC) observed in uncorrected OCTA (Fig. 4(E1)) were effectively eliminated by both the rule-based sacPR-OCTA (Fig. 4(E2)) and aiPR-OCTA (Fig. 4(E3)). Notably, in addition to presenting improved MNV vasculature, aiPR-OCTA demonstrates a cleaner outer retinal layer, particularly with the removal of projection artifacts (Fig. 4(F3)).

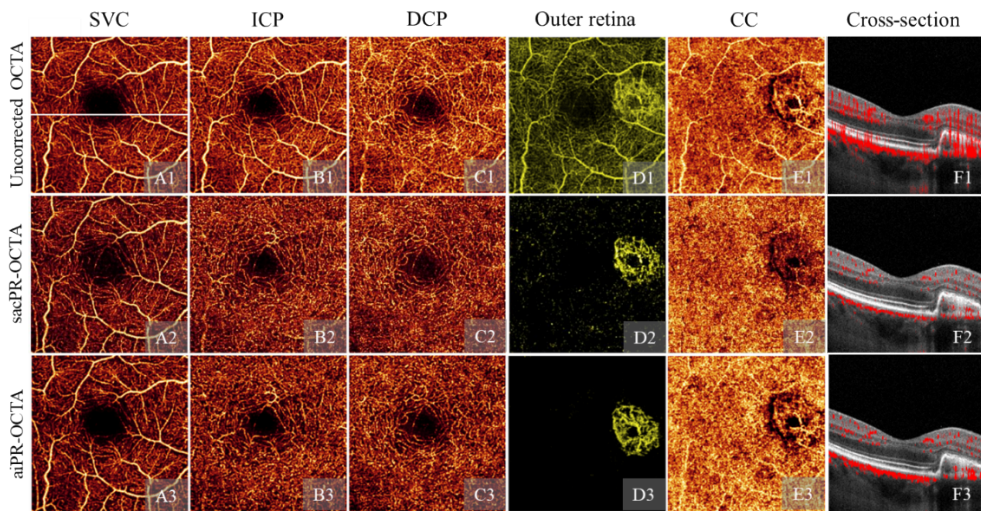


Fig. 4. A comparison of artifact removal algorithms on a scan with macular neovascularization (MNV): uncorrected OCTA (row 1), rule-based signal attenuation-compensated projection-resolved OCTA (sacPR-OCTA, row 2), and the artificial intelligence-assisted projection-resolved OCTA (aiPR-OCTA, row 3) showing *en face* OCT angiograms of the superficial vascular plexus (SVC, column A), the intermediate capillary plexus (ICP, column B), the deep capillary plexus (DCP, column C), the outer retina (column D) and the choriocapillaris (CC, column E), and the cross-sectional structural OCT overlaid with color-coded flow signal (column F; Red). The proposed aiPR-OCTA algorithm presented the best contrast and integrity of the *in situ* MNV signal. The dynamic display range, defined as [2.5th percentile, 97.5th percentile], was applied to generate uniformly displayed images, mitigating the brightness variation caused by differences in signal strength variation.

3.2.2. Preservation of angiomatous proliferation

Retinal angiomatous proliferation refers to the abnormal growth of blood vessels extending from the inner to the outer retina. [22–24] This pathology can manifest in various diseases, including age-related macular degeneration (AMD), diabetic retinopathy, and retinal vein occlusions. Angiomatous proliferation within the retina can lead to complications such as macular edema, hemorrhage, and eventual vision loss if left untreated. Accurate diagnosis of this condition is crucial for timely intervention. In uncorrected OCTA images (Fig. 5(D1)), angiomatous proliferation appears as vertical vessels connecting the inner and outer retina. However, interpretation can be complicated by projection artifacts, especially when these artifacts intersect with large vessels, making it challenging to distinguish *in situ* from false flow signals. The rule-based sacPR-OCTA method (Fig. 5(D2)) retains *in situ* flow signal from angiomatous proliferation but may still display some residual projection artifacts from large vessels. When these artifacts overlay with *in situ* signals, they can potentially impact automated segmentation accuracy. In contrast, aiPR-OCTA effectively preserves more genuine signals while removing residual projection artifacts from large vessels (Fig. 5(D3)), improving the clarity of the image and facilitating more accurate interpretation.

3.2.3. Cleaner NPA in diabetic retinopathy

NPA is a quantitative biomarker for characterizing ischemia in diabetic retinopathy (DR). However, noise in NPA can lead to incorrect quantification. By removing noise in NPA in the ground truth, the proposed model can learn this knowledge and generate a cleaner NPA

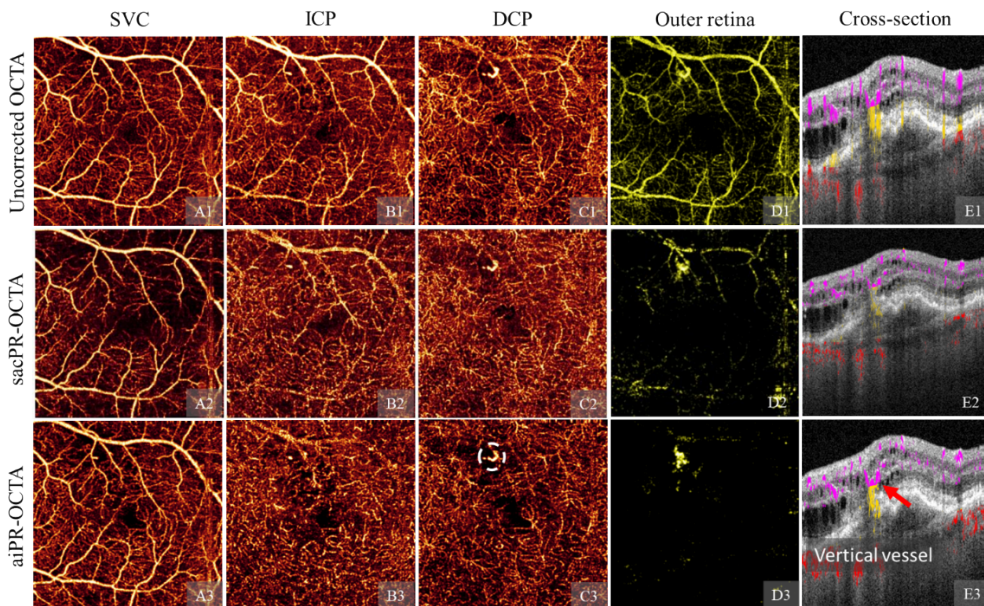


Fig. 5. A comparison of artifact removal algorithms on a scan with angiomatic proliferation (Type 3 MNV): uncorrected OCTA (row 1), rule-based signal attenuation-compensated projection-resolved OCTA (sacPR-OCTA, row 2), and the artificial intelligence-assisted projection-resolved OCTA (aiPR-OCTA, row 3) showing *en face* OCT angiogram of the superficial vascular plexus (SVC, column A), the intermediate capillary plexus (ICP, column B), the deep capillary plexus (DCP, column C), the outer retina (column D) and the choriocapillaris (CC, column E), and the cross-sectional structural OCT overlaid with color-coded flow signal (column F; violet: inner retina, yellow: outer retina red: choroid). The proposed aiPR-OCTA algorithm presented best contrast and integrity of the *in situ* angiomatic proliferation signal. The dynamic display range, defined as [2.5th percentile, 97.5th percentile], was applied to generate uniformly displayed images, mitigating the brightness variation caused by differences in signal strength variation.

in the output (Fig. 6(A3-D3)), in contrast to the uncorrected OCTA (Fig. 6(A1-D1)) and the rule-based sacPR-OCTA (Fig. 6(A2-D2)), where the impulse noise can be visualized in both. Both sacPR-OCTA and aiPR-OCTA effectively identify vascular abnormalities, such as dilated vessels and microaneurysms. The higher SNR in aiPR-OCTA reduces the challenges associated with quantifying these vascular abnormalities.

4. Discussion and conclusion

To the best of our knowledge, our team is the pioneer in devising an AI-assisted, volumetric projection artifact removal algorithm that effectively eliminates flow projection artifacts while conserving the *in situ* flow signal in OCTA images. This advancement over prior algorithms enhances the flow signal-to-noise ratio across all levels and facilitates the quantification of crucial disease metrics like vessel density, non-perfusion area, and MNV area.

The proposed aiPR-OCTA model exhibited reliable performance owing to several innovative features. Firstly, we collected a large real-world OCTA dataset from the clinic using two FDA-approved commercial OCTA devices that included healthy eyes and eyes afflicted with various retinal diseases, including AMD, DR, and rare diseases. This comprehensive dataset ensured thorough training of the model across diverse features. Secondly, the model benefited

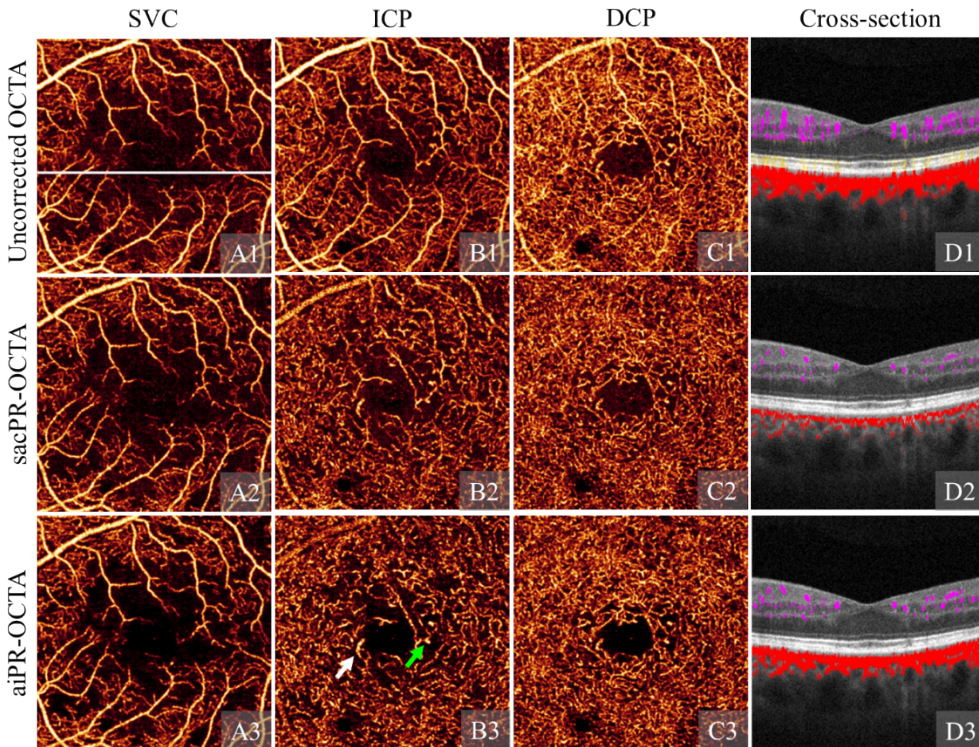


Fig. 6. A comparison of artifact removal algorithms on a scan with diabetic retinopathy (DR). uncorrected OCTA (row 1), rule-based signal attenuation-compensated projection-resolved OCTA (sacPR-OCTA, row 2), and the artificial intelligence-assisted projection-resolved OCTA (aiPR-OCTA, row 3) showing *en face* OCT angiogram of the superficial vascular plexus (SVC, column A), the intermediate capillary plexus (ICP, column B), the deep capillary plexus (DCP, column C), and the cross-sectional structural OCT overlaid with color-coded flow signal (column D; violet: inner retina, yellow: outer retina red: choroid) The proposed aiPR-OCTA algorithm presented cleaner NPA and preserved the vascular abnormalities including dilated vessel (white arrow highlighted) and microaneurysms (green arrow highlighted). The dynamic display range, defined as [2.5th percentile, 97.5th percentile], was applied to generate uniformly displayed images, mitigating the brightness variation caused by differences in signal strength variation.

from high-quality ground truth data generated via the semi-automated sacPR-OCTA algorithm, which effectively removed background noise, preserved *in situ* MNV signals, and generated complete choriocapillaris (CC) signals. Thirdly, the model was specifically designed to estimate proportion maps, enabling the restoration of *in situ* flow signals from coarse features, aligning with the principles of the PR-OCTA algorithm. This entailed the establishment of a complex non-linear relationship among *in situ* flow signals, detected flow signals (uncorrected OCTA), and OCT signals, achieved through extensive linear convolutions and non-linear activation functions. Lastly, we developed enhanced loss functions to guide the convergence of the AI model, ensuring more effective training and optimization.

A proficient algorithm is anticipated to effectively remove projection artifacts while preserving the *in situ* flow signals. To thoroughly evaluate the performance of the aiPR-OCTA algorithm, we employed three quantitative metrics—SSIM, fSNR, and remaining artifact strength. A lower SSIM value was anticipated to signify the removal of duplicated vascular patterns, while a higher

fSNR value was expected to indicate a cleaner background with a more prominent vascular signal. Additionally, a lower residual artifact strength was anticipated to indicate the successful removal of projection artifacts. Following the evaluation and demonstration of images, we concluded that the aiPR-OCTA model successfully removed projection artifacts and notably reduced background noise, while maintaining the integrity of the *in situ* flow signal with higher fSNR. Furthermore, aiPR-OCTA demonstrated improved background cleanliness in the outer retina, particularly evident in scans diagnosed with MNV and angiomatic proliferation, thereby providing enhanced images conducive to accurate diagnosis and quantification. aiPR-OCTA can both remove projection artifacts and clean the background, whereas sacPR-OCTA just gets you the projection artifact removal.

The proposed aiPR-OCTA model restores *in situ* flow signals from the original OCTA (uncorrected OCTA). The model was designed based on the nature of projection artifact formation, where artifacts are cast from slabs above along the A-line. As the CNN layers deepen, features are progressively down-sampled to extract relevant information while incorporating information from different depths. This ensures that information from the upper slabs and optical path length is accounted for estimating *in situ* flow signal proportion at each voxel. The fast scan direction was preserved to maintain the imaging resolution. Training aiPR-OCTA model is slower than the traditional tasks, such as classification or segmentation, in which either the presence of a feature is obvious or the number of features is often small. By comparison, training a network to remove projection artifacts volumetrically requires assessing an entire scan since these artifacts are always present in OCTA due to being a real manifestation of motion contrast. Furthermore, distinguishing between artifactual vessels and *in situ* vessels can be difficult. The seven years of experience of the graders on this project was instrumental in constructing a viable ground truth.

There are some limitations to this work. A large model would achieve a better performance. However, the training could be more difficult since the output of each voxel is a continuous value that varies between 0 and 1, and the training is way more difficult than training a classification or segmentation model with more limited output values. One more limitation of this work is that the model mainly processes the 3×3 -mm OCTA scans on the Optovue Avanti and Solix OCTA devices. It is possible that additional training would be required for the approach to achieve similar results in larger images or images from other devices. In the future, we will keep working to improve performance by collecting the training on the model using multiple OCTA devices, such as Zeiss Angioplex, Heidelberg Engineering, Topcon, etc., and retain the model to make it work on more OCTA scans, such 6×6 -mm, or larger size.

Funding. National Institutes of Health (R01 EY 036429, R01 EY035410, R01 EY024544, R01 EY027833, R01 EY031394, R43EY036781, P30 EY010572, T32 EY023211, UL1TR002369); Jennie P. Weeks Endowed Fund; Malcolm M. Marquis, MD Endowed Fund for Innovation; Unrestricted Departmental Funding Grant and Dr. H. James and Carole Free Catalyst Award from Research to Prevent Blindness (New York, NY); Edward N. & Della L. Thome Memorial Foundation Award, and the Bright Focus Foundation (G2020168, M20230081).

Disclosures. J. Wang, Visionix/Optovue (P, R), Roche/Genentech (P, R), Ifocus Imaging (I); T.T. Hormel, Ifocus Imaging (I); S. Bailey, Visionix/Optovue, Inc. (F); T.S. Hwang, None; Y. Jia: Visionix/Optovue (P, R), Roche/Genentech (P, R, F), Ifocus Imaging (I), Optos (P), Boeringer Ingelheim (C), Kugler (R).

Data availability. The OCTA Data presented in this paper is not publicly available for download but may be obtained from the authors upon reasonable request.

References

1. Y. Jia, O. Tan, J. Tokayer, *et al.*, “Split-spectrum amplitude-decorrelation angiography with optical coherence tomography,” *Opt. Express* **20**(4), 4710–4725 (2012).
2. L. An and R. K. Wang, “*In vivo* volumetric imaging of vascular perfusion within human retina and choroids with optical micro-angiography,” *Opt. Express* **16**(15), 11438–11452 (2008).
3. J. Campbell, M. Zhang, T. Hwang, *et al.*, “Detailed vascular anatomy of the human retina by projection-resolved optical coherence tomography angiography,” *Sci. Rep.* **7**(1), 42201–11 (2017).

4. Y. Jia, S. T. Bailey, D. J. Wilson, *et al.*, "Quantitative optical coherence tomography angiography of choroidal neovascularization in age-related macular degeneration," *Ophthalmology* **121**(7), 1435–1444 (2014).
5. R. Patel, J. Wang, J. P. Campbell, *et al.*, "Classification of choroidal neovascularization using projection-resolved optical coherence tomographic angiography," *Invest. Ophthalmol. Visual Sci.* **59**(10), 4285–4291 (2018).
6. J. Wang, T. T. Hormel, K. Tsuboi, *et al.*, "Deep learning for diagnosing and segmenting choroidal neovascularization in OCT angiography in a large real-world data set," *Trans. Vis. Sci. Tech.* **12**(4), 15 (2023).
7. S. T. Bailey, O. Thaware, J. Wang, *et al.*, "Detection of nonexudative choroidal neovascularization and progression to exudative choroidal neovascularization using OCT angiography," *Ophthalmology Retina* **3**(8), 629–636 (2019).
8. R. F. Spaide, J. G. Fujimoto, and N. K. Waheed, "Image artifacts in optical coherence tomography angiography," *Retina* **35**(11), 2163–2180 (2015).
9. A. Zhang, Q. Zhang, and R. K. Wang, "Minimizing projection artifacts for accurate presentation of choroidal neovascularization in OCT micro-angiography," *Biomed. Opt. Express* **6**(10), 4130–4143 (2015).
10. M. Zhang, T. S. Hwang, J. P. Campbell, *et al.*, "Projection-resolved optical coherence tomographic angiography," *Biomed. Opt. Express* **7**(3), 816–828 (2016).
11. J. Wang, M. Zhang, T. S. Hwang, *et al.*, "Reflectance-based projection-resolved optical coherence tomography angiography," *Biomed. Opt. Express* **8**(3), 1536–1548 (2017).
12. J. Wang, T. T. Hormel, S. T. Bailey, *et al.*, "Signal attenuation-compensated projection-resolved OCT angiography," *Biomed. Opt. Express* **14**(5), 2040–2054 (2023).
13. M. Zhang, J. Wang, A. D. Pechauer, *et al.*, "Advanced image processing for optical coherence tomographic angiography of macular diseases," *Biomed. Opt. Express* **6**(12), 4661–4675 (2015).
14. J. Wang, T. T. Hormel, L. Gao, *et al.*, "Automated diagnosis and segmentation of choroidal neovascularization in OCT angiography using deep learning," *Biomed. Opt. Express* **11**(2), 927–944 (2020).
15. J. Wang, T. T. Hormel, Q. You, *et al.*, "Robust non-perfusion area detection in three retinal plexuses using convolutional neural network in OCT angiography," *Biomed. Opt. Express* **11**(1), 330–345 (2020).
16. Z. Wang, A. C. Bovik, H. R. Sheikh, *et al.*, "Image quality assessment: from error visibility to structural similarity," *IEEE Trans. on Image Process.* **13**(4), 600–612 (2004).
17. L. A. Donoso, D. Kim, A. Frost, *et al.*, "The role of inflammation in the pathogenesis of age-related macular degeneration," *Surv. Ophthalmol.* **51**(2), 137–152 (2006).
18. P. E. Stanga, J. I. Lim, and P. Hamilton, "Indocyanine green angiography in chorioretinal diseases: indications and interpretation: an evidence-based update," *Ophthalmology* **110**(1), 15–21 (2003).
19. Q. Zhang, A. Zhang, C. S. Lee, *et al.*, "Projection artifact removal improves visualization and quantitation of macular neovascularization imaged by optical coherence tomography angiography," *Ophthalmology retina* **1**(2), 124–136 (2017).
20. F. Corvi, M. Cozzi, E. Barbolini, *et al.*, "Comparison between several optical coherence tomography angiography devices and indocyanine green angiography of choroidal neovascularization," *Retina* **40**(5), 873–880 (2020).
21. N. J. Y. Yeo, E. J. J. Chan, and C. Cheung, "Choroidal neovascularization: mechanisms of endothelial dysfunction," *Front. Pharmacol.* **10**, 491457 (2019).
22. K. V. Bhavsar, Y. Jia, J. Wang, *et al.*, "Projection-resolved optical coherence tomography angiography exhibiting early flow prior to clinically observed retinal angiomatic proliferation," *American Journal of Ophthalmology Case Reports* **8**, 53–57 (2017).
23. A. S. Tsai, N. Cheung, A. T. Gan, *et al.*, "Retinal angiomatic proliferation," *Surv. Ophthalmol.* **62**(4), 462–492 (2017).
24. L. A. Yannuzzi, S. Negrão, T. Iida, *et al.*, "Retinal angiomatic proliferation in age-related macular degeneration," *Retina* **21**(5), 416–434 (2001).